



# Design of a Finger-Sized Voice Coil Motor for High-Speed Scanners

Sunghoon Kang<sup>1</sup> · Yong-Gon Jeong<sup>2</sup> · Young-Man Choi<sup>2</sup>

Received: 3 February 2022 / Revised: 13 March 2022 / Accepted: 30 March 2022 / Published online: 2 December 2022  
© The Author(s), under exclusive licence to Korean Society for Precision Engineering 2022

## Abstract

Voice coil motor (VCM) is a versatile high-precision actuator for miniaturization of electronic devices such as auto-focusing unit for cell-phone cameras and pickup actuators in hard disk drives. VCM can be also applied to hand-held medical devices in a slender and cylindrical shape. For a miniaturized design, of which size is comparable to human finger, it is crucial to make thrust force uniform over its moving range and power optimized. In this study, we propose a miniaturized cylindrical VCM with symmetric stator. The symmetric arrangement has advantages of enhancing uniformity of magnetic flux density in the air gap and reducing leakage flux due to its closed form. However, leakage flux between yokes inside the actuator still affects the thrust force, which is critical for a miniaturized design. Considering this leakage flux, a magnetic equivalent circuit model of the VCM is developed and verified by comparing with finite element analysis. We optimized the proposed VCM to maximize the slenderness for miniaturization with a stroke of 10 mm. Fabricated VCM was of 13 mm diameter and 40 mm length. Measured magnetic flux density and force constant are well matched with the model prediction. Finally, we built a high-speed linear scanner to verify the performance of the VCM. For a 10-Hz sinusoidal trajectory, the tracking error was less than  $\pm 35 \mu\text{m}$  in RMS value. During full-stroke scanning, the temperature of coil was maintained at 34.5 °C.

**Keywords** Voice coil motor · Permeance method · Magnetic equivalent circuit · Magnetic leakage flux

## 1 Introduction

Voice coil motor (VCM) is a type of actuator which uses Lorentz force and has been used widely in precision motion systems. It has advantages such as large motion range and high-speed response. Furthermore, having linear relationship between input current and output force and being free from friction and backlash, high precision and reliability of VCM has been utilized in focusing unit for laser scanners [1], auto-focusing actuator in portable devices [2], hard disk drive [3], nano positioning stage [4, 5], vibration compensation [6], fast steering mirror [7] and die bonder [8]. Researchers have found that VCM can be manufactured in various shapes and sizes so that there have been various studies on applying VCM to small devices such as optical pickup actuator for optical disk drives and auto focusing unit for mobile phone

camera. In the field of medical devices, VCM has been used in endoscopes and surgical robots [9] and scanning device for optical components in dental medicine [10, 11]. In these applications, actuators are required to have small diameter with large motion range which makes them have high aspect ratio or high slenderness.

VCMs are usually designed as an open-end type as shown in Fig. 1a for easy assembly. This arrangement, however, is prone to magnetic leakage flux and loss of thrust force. Moreover, there is inevitable force variation in its motion range due to the asymmetry of the magnetic flux. As the VCM in this type becomes smaller, these effects are more crucial. To alleviate this issue, VCMs with symmetric structure have been studied [12, 13]. In this structure, the magnetic leakage flux does not occur as shown in Fig. 1b. In addition, more uniform magnetic flux in the air gap can be obtained. Instead of two opposing magnets [12], single radially magnetized magnet [13] can be used for the symmetric configuration.

In this study, we propose a finger-sized cylindrical VCM for high-speed scanners. The symmetric arrangement enables large stroke and small size as well as reduces the magnetic leakage flux and enhances the uniformity of magnetic

✉ Young-Man Choi  
ymanchoi@ajou.ac.kr

<sup>1</sup> Department of Mechanical and Control Engineering, Seoul Cyber University, Seoul, Republic of Korea

<sup>2</sup> Department of Mechanical Engineering, Ajou University, Suwon, Gyeonggi-do, Republic of Korea

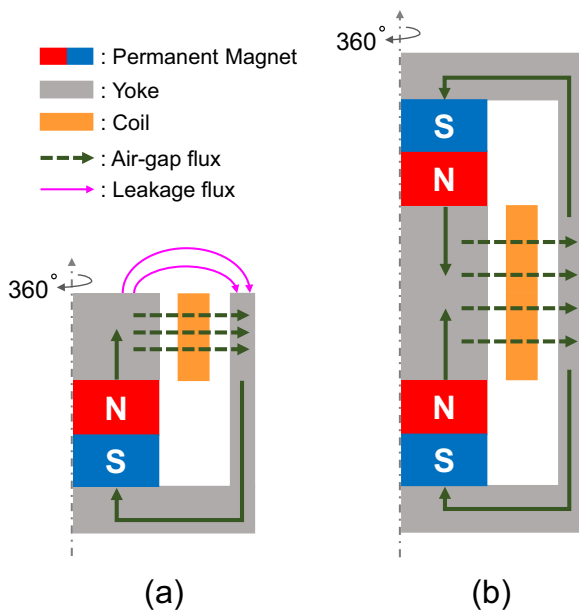


**Fig. 1** VCM structure (a) open-end type (b) symmetric type

flux. We established an accurate magnetic circuit model of the proposed VCM by determining the leakage flux. The model is verified by comparing with finite element analysis (FEA). Using the model, the proposed VCM is optimized to maximize the slenderness for miniaturization. The remainder of this study is organized as follows: Sect. 2 describes the development of magnetic circuit model. Layout and result of optimization is presented in Sect. 3. Performance of fabricated VCM is assessed in Sect. 4, and conclusions are summarized in Sect. 5.

## 2 Modeling of the VCM

### 2.1 Magnetic Equivalent Circuit Model

Due to the cylindrical and symmetric manner of structure, the proposed VCM can be simplified to a quarter part of the whole structure as shown in Fig. 2a with geometric parameters. Permeance method was used to model the proposed VCM. Permeance method, which is a simple way to model a VCM as a magnetic equivalent circuit, has been used in various studies [1, 6, 8, 14]. In spite of lack of accuracy compared to FEA, permeance method is superior in fast calculation and convenience which is favorable for optimization. Permeance indicates how well the magnetic flux can flow in a material and can be considered as a reciprocal of reluctance in a magnetic circuit. Components of VCM such as yokes, permanent magnet, and air gap can be thought of as paths of magnetic flux. While the magnetic leakage flux at the open-end is removed due to the structural symmetry,

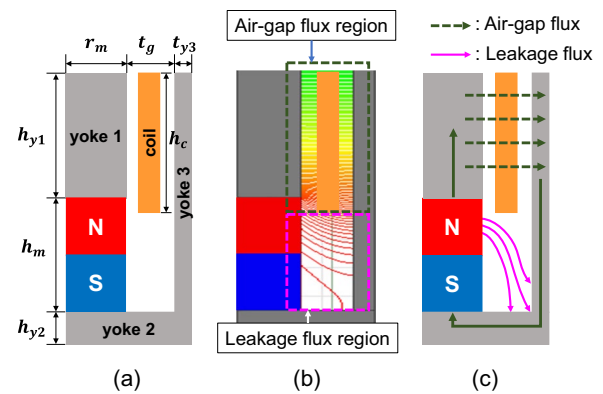


**Fig. 2** Conceptual design of the proposed VCM (a) geometric parameters (b) magnetic flux diagram from FEA (c) magnetic leakage flux

there is still another type of leakage flux which does not pass through the coil, goes from the top of the magnet to the side yoke and bottom yoke as depicted in Fig. 2b. Inaccuracy of permeance method comes from insufficient consideration of leakage fluxes [15, 16]. Thus, in order to enhance the accuracy of magnetic equivalent circuit, it is of great importance to examine the effect of this type of leakage flux which was absent from previous studies [1, 14, 15]. For simplicity, the magnetic flux from the magnet can be regarded to be divided into an air-gap flux and leakage flux as shown in Fig. 2c.

Based on this idea, Fig. 3 shows the magnetic equivalent circuit for the proposed VCM. The permanent magnet is modelled as a magnetic flux source  $\Phi_r$ , and magnet's own permeance  $P_m$ . There are two loops in the circuit: One is the main loop which passes through the permanent magnet, center yoke, air gap, side yoke, and bottom yoke. The other is a loop of leakage flux. We assume the leakage flux in

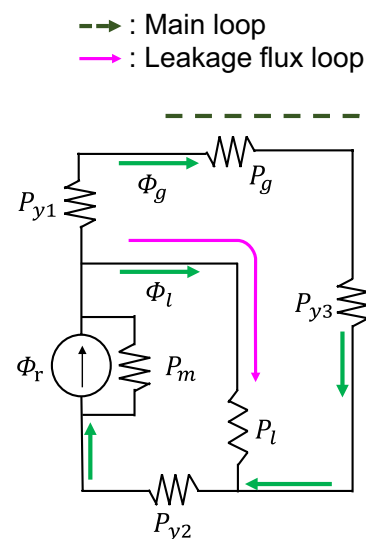


**Fig. 3** Magnetic equivalent circuit model for the proposed VCM

Fig. 2c flows directly from the magnet to the bottom yoke. It is indicated as a leakage permeance  $P_l$  in Fig. 3. The magnetic flux through the air gap, and through the leakage path are denoted as  $\Phi_g$ , and  $\Phi_l$ , respectively. Permeance of each component was calculated using equations which can be found in [17]:

- Permanent magnet:

$$P_m = \frac{\pi \mu_0 \mu_r r_m^2}{h_m} \quad (1)$$

- Center yoke:

$$P_{y1} = \frac{\pi \mu_0 \mu_s r_m^2}{h_{y1}} \quad (2)$$

- Bottom yoke:

$$P_{y2} = \frac{2\pi \mu_0 \mu_s h_{y2}}{\ln(r_m + t_g + t_{y3}/2) - \ln(r_m/2)} \quad (3)$$

- Side yoke:

$$P_{y3} = \frac{\pi \mu_0 \mu_s \{(r_m + t_g + t_{y3})^2 - (r_m + t_g)^2\}}{h_{y1} + h_m} \quad (4)$$

- Air gap:

$$P_g = \frac{2\pi \mu_0 h_{y1}}{\ln(r_m + t_g) - \ln(r_m)} \quad (5)$$

- Leakage flux:

$$P_l = 0.52 \times (2\pi \mu_0 r_m) \quad (6)$$

where  $\mu_0$ ,  $\mu_r$ ,  $\mu_s$  are permeability of vacuum, magnet, and steel, respectively.

Applying the Kirchhoff's law, the magnetic flux in the air gap,  $\Phi_g$ , is obtained as

$$\Phi_g = \Phi_r \frac{1}{P_m P_l \left( \frac{1}{P_m} + \frac{1}{P_{y2}} + \frac{1}{P_*} \right)} \times \frac{1}{\left( \frac{1}{P_l} + \frac{1}{P_g} + \frac{1}{P_{y1}} + \frac{1}{P_{y3}} \right)} \quad (7)$$

where

$$P_* = \frac{1}{\frac{1}{P_g} + \frac{1}{P_{y1}} + \frac{1}{P_{y3}}} + P_l \quad (8)$$

The magnetic flux density in the air gap, which is proportional to the thrust force of VCM, is calculated by

$$B_g = \frac{\Phi_g}{A_g} \quad (9)$$

where  $A_g$  is the effective area of the air gap.

## 2.2 Coil Parameters and Heat Exchange Model

Given the coil and winding parameters, the number of coil turns and heat exchange model was established to determine the performance of VCM. Figure 4 shows the design parameters of coil winding where  $w_c$  and  $h_c$  are the width and height of coil winding, respectively, and  $d_c$  is the bare coil diameter.

Total number of coil turns was given as

$$n = \left[ \frac{h_c}{d_c^*} \right] \left[ \frac{2}{\sqrt{3}} \frac{w_c}{d_c^*} \right] \quad (10)$$

where  $d_c^*$  is the coil diameter including enamel coating which satisfies  $d_c^* = r_p \times d_c$  where  $r_p$  is the packing ratio, and  $[x]$  is the largest integer not greater than  $x$ .

Heat generated from the coil should be examined because it may alter the performance of VCM. For example, the resistance of copper increases due to overheating, and the magnetic flux from permanent magnet may be influenced by the temperature change. Resistance of coil could be evaluated as

$$R_c = \frac{\rho_{cu} n L_m}{(\pi/4) d_c^2} \quad (11)$$

where  $\rho_{cu}$  is resistivity of copper,  $c_c$  and  $t_b$  are clearance of coil and thickness of bobbin, respectively, and  $L_m$  is the mean length of coil which was given as

$$L_m = 2\pi(r_m + c_c + t_b + w_c/2) \quad (12)$$

Heat exchange model of our VCM is depicted in Fig. 5. Heat generated from coil can be calculated simply by

$$Q_g = I^2 R_c \quad (13)$$

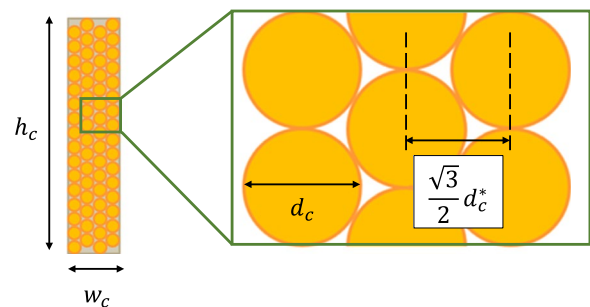
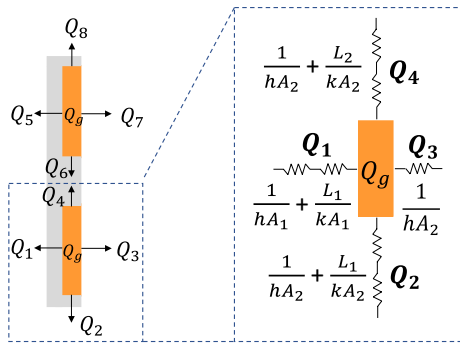
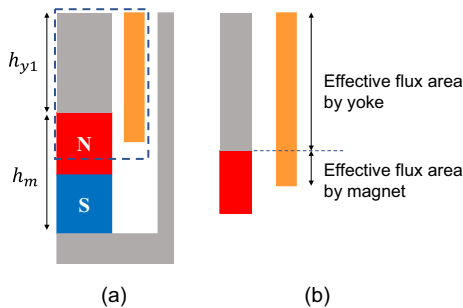


Fig. 4 Design parameters of coil winding



**Fig. 5** Heat exchange model of the coil part of the VCM



**Fig. 6** Effective coil area for calculation of thrust force (a) coil winding of overhung type (b) effective flux area by yoke and magnet

where  $I_c$  is the coil current. Total heat dissipation is the sum of heat dissipation at eight sides as shown in Fig. 5,

$$Q_d = \sum_{i=1}^8 Q_i \quad (14)$$

Heat dissipation at each side is obtained by

$$Q_i = \frac{T_c - T_{amb}}{(1/hA_i + L_i/kA_i)} \quad (15)$$

where  $T_c$  and  $T_{amb}$  are temperature of coil and ambient air, respectively,  $L_i$  is length of  $i$ -th side,  $A_i$  is area of  $i$ -th side,  $h$  is the heat convection coefficient of air, and  $k$  is the heat conduction coefficient of bobbin. Convection and conduction coefficients were estimated to be 10 W/m<sup>2</sup>K and 0.19 W/mK, respectively.

### 2.3 VCM Thrust Force Model

In order to enhance the thrust force, the proposed VCM was designed as an overhung type as shown in Fig. 6a in which some part of coil is outside the air gap area around the center yoke. This part of coil also contributes to the thrust force

due to fringing effect of the flux from magnet. To consider this part, an effective number of coil turns were introduced, which is given as

$$n_{eff} = \frac{(h_{y1} - h_b) + 0.08h_m}{h_c} \cdot n \quad (16)$$

where  $h_b$  is the height of bobbin. To derive the heuristic relationship, FEA was conducted for various combinations of two design parameters,  $h_{y1}$  and  $h_m$ . The term of magnet height in (16) is included because the magnet height affects the effective flux area producing more fringing flux through the gap as shown in Fig. 6b. Finally, thrust force of VCM can be computed by

$$F_{VCM} = n_{eff} B_g L_m I_c \quad (17)$$

### 2.4 Modeling Verification and Parametric Study

The magnetic circuit model for the VCM was verified by comparing the magnetic flux density and thrust force from the model with those from FEA (ANSYS Multiphysics, ANSYS, USA). Two identical permanent magnets (NdFeB N35) of 1.17 T remanence and 867 kA/m coercive force are used. AISI 1010 is assumed as the material of yokes with yoke saturation as 1.8 T and relative permeability as 1400.

Three design parameters of magnet radius, height of magnet and height of center yoke were investigated for verification. Having little effect to the performance of VCM, height of bottom yoke and thickness of side yoke were not considered as design parameters and selected to have appropriate dimensions to avoid magnetic flux saturation. Other parameters are given below:

- Gap between coil and stator: 0.4 mm
- Coil diameter: 0.26 mm
- Packing ratio: 1.15
- Width of coil winding: 1.2 mm
- Coil current: 1 A.

Figure 7a, b show the effect of magnet radius for three different values of height of magnet on the magnetic flux density in the air gap and thrust force of actuator, respectively. It clearly shows that the flux density and thrust force increases for larger magnet radius. Magnetomotive force of a permanent magnet, which is the magnetic flux source in magnetic equivalent circuit, is proportional to the cross-section area of magnet. Therefore, it can be expected that the larger magnet radius would cause the higher flux density and thrust force. Accuracy of permeance method was estimated by comparing the result of model with that of FEA. As shown in Fig. 7c, d, the error of proposed model is much smaller than that of

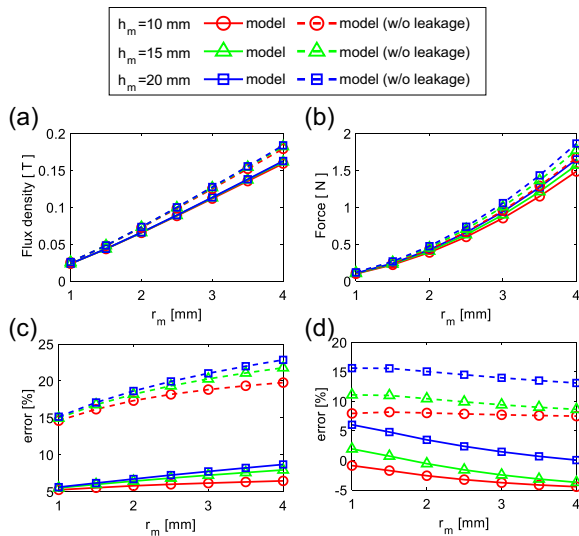


**Fig. 7** Effect of magnet radius on (a) averaged magnetic flux density at the air gap (b) thrust force (c) error for flux density at the air gap (d) error for thrust force

model without a consideration of leakage permeance. The magnetic circuit model and FEA are well matched with the maximum error of 8.7% and 6.0% for magnetic flux and thrust force, respectively.

Next, the height of center yoke is examined in Fig. 8. Higher center yoke decreases both the permeance of center yoke and flux density which can be derived from (2) and (7)–(9). Nevertheless, the thrust force increases with respect to height of center yoke since the coil winding height

depends on the height of center yoke and the number of coil turns increases for higher coil winding. As in the case of magnet radius, the proposed model is much more accurate than the model without leakage flux as shown in Fig. 8c, d. In this case, maximum error between the proposed model and FEA were 6.7% and –7.3% for flux density and thrust force, respectively.

Finally, for the magnet height as shown in Fig. 9a, the flux density is almost irrelevant to magnet height because the permeance of magnet is negligible compared to those of yokes. Thrust force is weakly proportional to magnet height because of its contribution to the effective number of coil turns as shown in (16). From Fig. 9c, d, it can be seen that the consideration of leakage flux enhances the accuracy of magnetic circuit model. Comparing the result of proposed model with FEA, the maximum error was 5.8% and 4.2% for flux density and thrust force, respectively.

### 3 Optimization

As a design example of our cylindrical miniaturized VCM, we optimized the VCM with a design objective to maximize its slenderness, i.e., the aspect ratio. The objective function of optimization was determined as

$$J = \min \left( \frac{r_{VCM}}{h_{VCM}} \right) \quad (18)$$

where  $r_{VCM} = r_m + t_g + t_{y3}$  and  $h_{VCM} = h_m + h_{y1} + h_{y2}$ . The motion range of the VCM is determined to  $\pm 5$  mm. Maximum thrust force requirement was set to 0.7 N as an

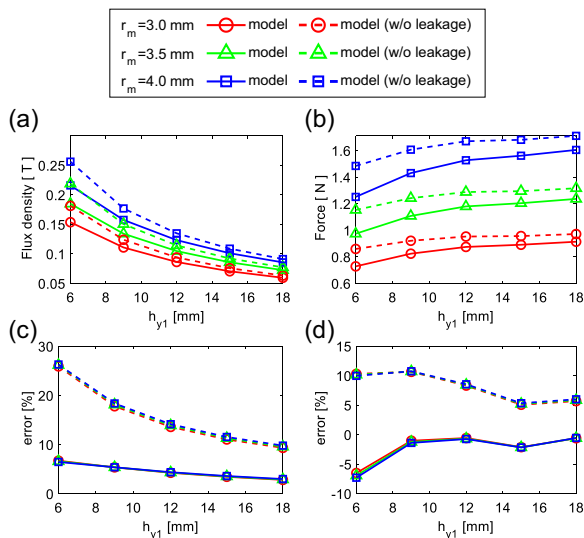


**Fig. 8** Effect of center yoke height on (a) averaged magnetic flux density at the air gap (b) thrust force (c) error for flux density at the air gap (d) error for thrust force

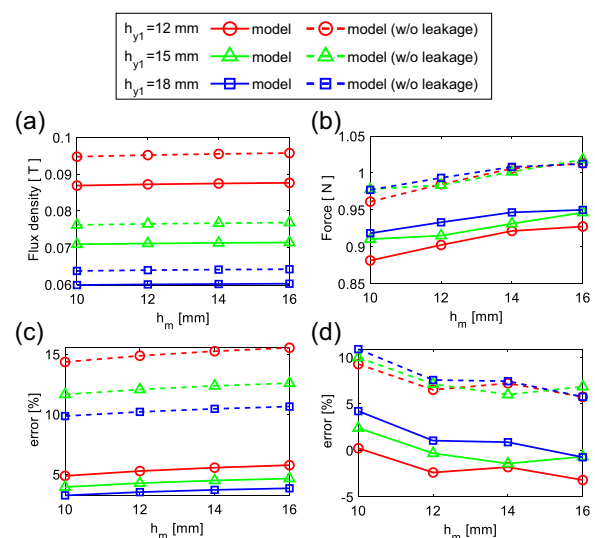


**Fig. 9** Effect of magnet height on (a) averaged magnetic flux density at the air gap (b) thrust force (c) error for flux density at the air gap (d) error for thrust force



equality constraint, while the maximum coil current was set to 1.0 A. Maximum coil temperature, which is determined from maximum coil current, was constrained to 100 °C. It is preferable to avoid the saturation of magnetic flux in yokes. Maximum magnetic flux density in yokes was constrained considering a factor of safety. Dimensions those have little effect to the performance of VCM such as thickness of side yoke and height of bottom yoke were properly chosen considering the manufacturability. Constraints are summarized as follows:

- (1) Maximum thrust force = 0.7 N

$$c_1 = F_{VCM} - 0.7 = 0 \quad (19)$$

- (2) Maximum coil current ≤ allowable maximum coil current

$$c_2 = I_{c,max} - 1.0 \leq 0 \quad (20)$$

- (3) Maximum coil temperature ≤ allowable maximum temperature

$$c_3 = T_{coil} - 100 \leq 0 \quad (21)$$

- (4) Maximum magnetic flux density of yoke ≤ saturation flux density

$$c_4 = \max(B_{y1}, B_{y2}, B_{y3}) \cdot K - 1.8 \leq 0 \quad (22)$$

- (5) Dimensional constraints as listed in Table 1 where  $K$  is a factor of safety for yoke saturation and  $B_{yi}$  is magnetic flux density of  $i$ -th yoke.

Dimensional constraints are designated considering the machinability, assembly tolerance, performance of VCM and miniaturization. For example, thin yokes are preferable for a miniaturized design while too thin yokes are not preferable because of saturation of magnetic flux and structural rigidity of VCM. Thickness of air gap and coil winding is needed to be as small as possible for a slender design of actuator. However, too thin air gap may cause problems of tight assembly tolerance or interference. Wide coil winding means high number of coil turns and high thrust force. Therefore, it would be beneficial to make the coil winding as wide as possible considering the thickness of air gap, radius of VCM, and tolerance of manufacturing and assembly.

The optimization was performed by sequential quadratic programming algorithm, which is a constrained nonlinear optimization algorithm and has been widely used in various studies [1, 4, 6], using a commercial software (MATLAB, Mathworks, USA). Convergence of design parameters and cost function is shown in Fig. 10. As a result, magnet radius, height of center yoke, and height of magnet are optimized to 2.98 mm, 9 mm, and 8 mm, respectively. The magnet

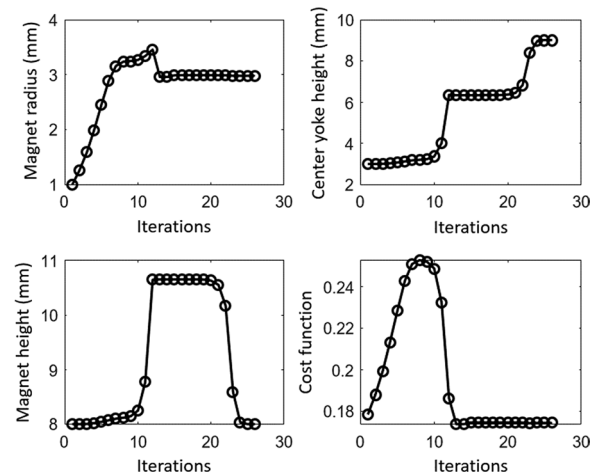


Fig. 10 Convergence of design parameters and cost function

Table 1 Dimensional constraints for optimization

Constraint	Dimension of VCM
$1 \text{ mm} \leq r_m \leq 4 \text{ mm}$	Magnet radius
$3 \text{ mm} \leq h_{y1} \leq 21 \text{ mm}$	Height of center yoke
$8 \text{ mm} \leq h_m \leq 22 \text{ mm}$	Height of magnet
$h_{VCM} \leq 40 \text{ mm}$	Height of VCM
$t_g = 2.5 \text{ mm}$	Thickness of air gap
$t_{y3} = 1 \text{ mm}$	Thickness of side yoke
$h_{y2} = 3 \text{ mm}$	Height of bottom yoke
$w_c = 1.2 \text{ mm}$	Width of coil winding
$h_g = 6 \text{ mm}$	Distance of bottom of coil winding from top of the bottom magnet
$d_c^* = 0.26 \text{ mm}$	Coil diameter with enamel coating

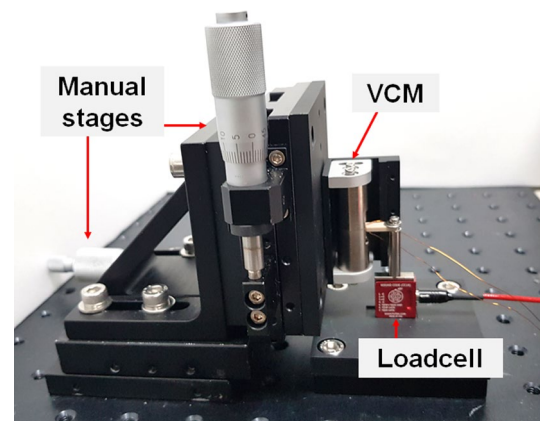
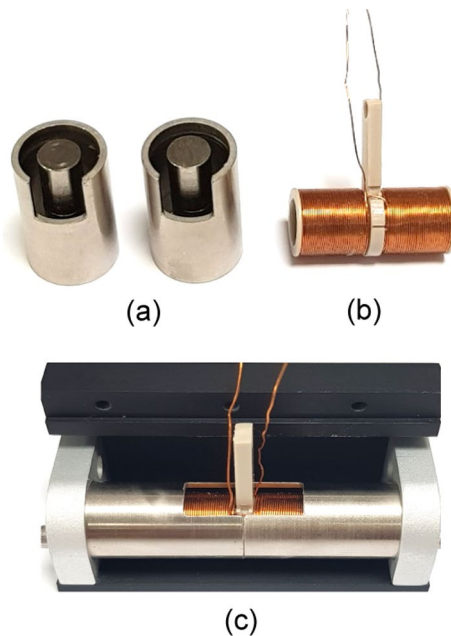
radius was adjusted to 3.0 mm for machinability. The final design of VCM had 13.0 mm diameter and 40.0 mm height. Parameters derived from the optimized design variables are outlined in Table 2.

## 4 Fabrication and Experimental Results

Figure 11 shows the fabricated parts of VCM and assembly. Stator yoke was manufactured from AISI 1020 steel as two symmetric parts with a slot on a side which is used for attachment. The slot has a negligible effect on the thrust force, which is confirmed less than 4% decrease by 3D FEM. A cylindrical magnet (NdFeB N35) was assembled with each stator yoke. The bobbin was manufactured of polyether ether ketone (PEEK) of 0.5 mm thickness. Total weight of the coil part is only 4.1 g. Resistance and inductance of coil was measured by an LCR meter (U1733, KEYSIGHT, USA) and had the values of 3.86 Ω and 0.31 mH, respectively.

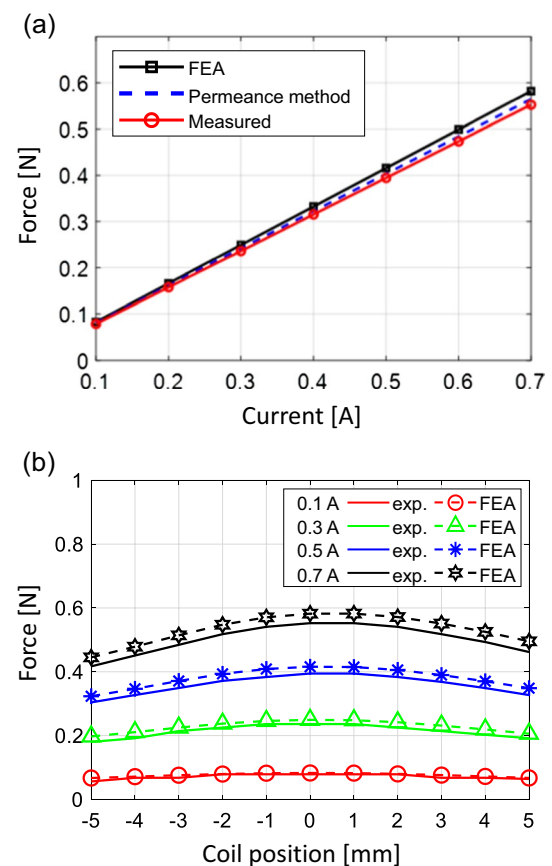
**Table 2** Final design parameters of VCM

Parameters	Value
Diameter of VCM	13 mm
Height of VCM	40 mm
Total number of coil turns	304
Height of coil winding (half part)	10 mm
Magnetic flux density in the air gap	108.3 mT
Maximum coil current	0.76 A
Force constant	0.91 N/A

**Fig. 12** Experiment setup to measure the thrust force of VCM**Fig. 11** Fabricated VCM (a) two stators (b) coil bobbin and windings (c) assembled VCM

Magnetic flux density in the air gap was measured by a gauss meter (TM-701, KANETEC, Japan) and had a value of 102.1 mT. It had an error of 3.0% compared to FEA result which was 105.3 mT, and 5.7% compared to the results of permeance model which was 108.3 mT.

To measure the thrust force of VCM, the coil part was fixed with a loadcell (LSB205, FUTEK, USA) using an auxiliary part, and position of the stator was adjusted by manual positioning stages as shown in Fig. 12. Vertical stage was to place the moving coil at the center of motion range. The VCM has a force constant of 0.79 N/A which agrees well with both results from the FEA and permeance model as shown in Fig. 13a. Over the entire motion range, the variation of thrust force was measured for coil current of 0.1 A, 0.3 A, 0.5 A, and 0.7 A as shown in Fig. 13b. The maximum

**Fig. 13** Thrust force measurement (a) force-to-current (b) force uniformity

force variation was 26.9% of the nominal force. Though this value is slightly larger than that of a conventional open-end type VCM [18], it is much smaller than other types of VCMs [19, 20]. The reason of force variation seems that the opening of the yoke part for the external fixture affects the saturation of the yoke when the coil is at the ends of the

motion range. Considering its slender form factor, the force uniformity of the proposed VCM is noteworthy.

To evaluate the dynamic performance, which is one of the major advantages of VCM, an experimental setup was established as shown in Fig. 14. A linear motion system consisting of LM guides (M-R-5MN, CPC, Taiwan), optical encoder (PIA-0100, Celeria Motion, USA) and VCM was built. A controller (DZRALTE-012L080, AMC, USA) was used for closed-loop position control. Figure 15 shows the result of 10-Hz sinusoidal tracking with an amplitude of 5 mm. Peak-to-peak and RMS values of tracking error were less than  $\pm 70 \mu\text{m}$  and  $\pm 35 \mu\text{m}$ , respectively.

Drive current of VCM for sinusoidal tracking is shown in Fig. 16a. It has a peak amplitude of 430 mA and RMS power consumption was 0.32 W. To assess the validity of heat exchange model, the coil temperature during the tracking test was monitored by a thermal imaging camera (A325sc, FLIR Systems, USA) as shown in Fig. 16b. Coil temperature was saturated at  $34.5^\circ\text{C}$  while the expected temperature was  $45.4^\circ\text{C}$  from (5)–(7). This discrepancy might be due to the convective cooling effect being stronger than expected because of high-speed VCM operation.

## 5 Conclusions

In this paper, a miniaturized cylindrical VCM was proposed. It had a symmetric arrangement to reduce magnetic leakage flux and enhance the magnetic flux density at the air gap. Also, we developed a magnetic equivalent circuit model considering the magnetic leakage flux and effective gap flux area. The model of VCM was verified by comparing the result of model with that of FEA. The proposed VCM was optimized to have high slenderness of 13 mm diameter and 40 mm height. Force constant of fabricated VCM was measured as 0.79 N/A which fit well with permeance model and FEA. A linear motion system was constructed to test the dynamic performance. Sinusoidal tracking with 10 Hz frequency and  $\pm 5$  mm motion range resulted in the tracking

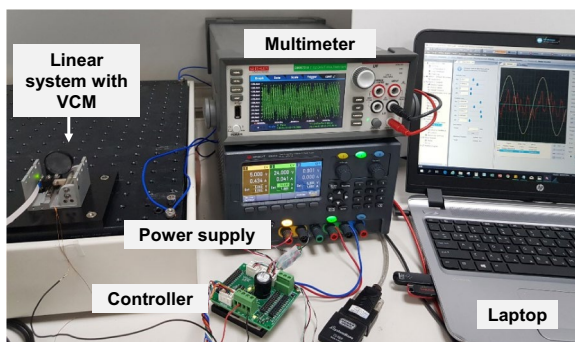


Fig. 14 Experimental setup for tracking test

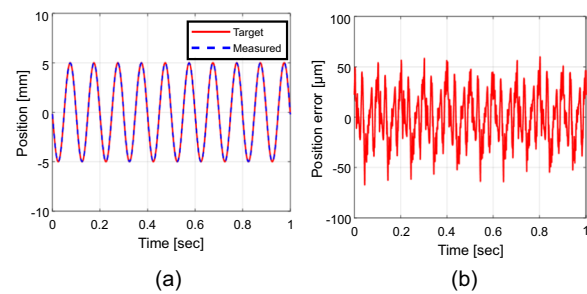


Fig. 15 Experimental results of 10 Hz full-stroke sinusoidal tracking (a) target and measured position (b) position error

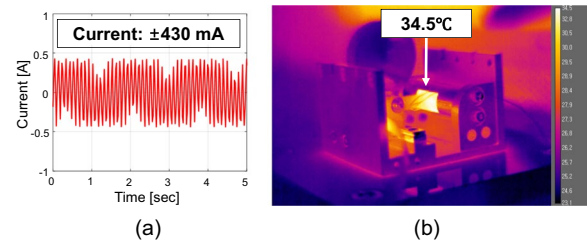


Fig. 16 Power consumption performances for sinusoidal tracking (a) measured current (b) infrared image of the VCM during the tracking

error less than  $\pm 70 \mu\text{m}$  in peak-to-peak and  $\pm 35 \mu\text{m}$  in RMS value. Steady-state temperature of VCM was measured as  $34.5^\circ\text{C}$  during the tracking test, which was satisfactory for a high-speed operation.

**Acknowledgements** This study is funded by Dentium Co. Ltd. and Ajou University.

## Declarations

**Competing Interests** The authors declare that they have no competing interests.

## References

1. Lee, M. G., Kim, G., Lee, C.-W., Lee, S.-H., & Jeon, Y. (2014). Design of voice coil motor dynamic focusing unit for a laser scanner. *Review of Scientific Instruments*, 85(4), 045104. <https://doi.org/10.1063/1.4869339>
2. Liu, C. S., & Lin, P. D. (2009). Miniaturized auto-focusing VCM actuator with zero holding current. *Optics Express*, 17(12), 9754–9763. <https://doi.org/10.1364/OE.17.009754>
3. Choi, Y. M., Ahn, D., Gweon, D. G., & Jeong, J. (2010). Halbach magnetic circuit for voice coil motor in hard disk drives. *Journal of Magnetism*, 15(3), 143–147. <https://doi.org/10.4283/JMAG.2010.15.3.143>
4. Ahn, D., Choi, Y. M., & Jeong, J. (2015). Design of a four-degree-of-freedom nano positioner utilizing electromagnetic actuators and flexure mechanisms. *Review of Scientific Instruments*, 86(3), 035101. <https://doi.org/10.1063/1.4908128>
5. Shan, G., Li, Y., Zhang, L., Wang, Z., Zhang, Y., & Qian, J. (2015). Contributed Review: Application of voice coil motors

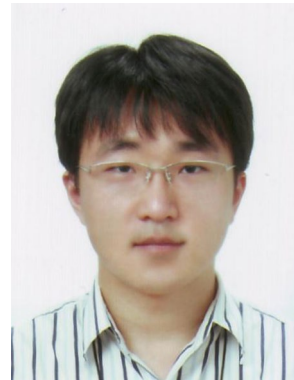


- in high-precision positioning stages with large travel ranges. *Review of Scientific Instruments*, 86(10), 101501. <https://doi.org/10.1063/1.4932580>
6. Choi, Y. M., Ahn, D., Gweon, D. G., & Lee, M. G. (2016). Design of a rectangular-type voice coil actuator for frame vibration compensation. *Journal of Magnetism*, 21(3), 348–355. <https://doi.org/10.4283/JMAG.2016.21.3.348>
  7. Xiao, R., Xu, M., Shao, S., & Tian, Z. (2019). Design and wide-bandwidth control of large aperture fast steering mirror with integrated-sensing unit. *Mechanical Systems and Signal Processing*, 126, 211–226. <https://doi.org/10.1016/j.ymssp.2019.02.028>
  8. Lou, Y., Yang, X., Li, K., & Zhao, X. (2013). Design and optimization of a linear voice coil motor for LED die bonders. In *2013 IEEE international conference on information and automation (ICIA)* (pp. 1011–1016). IEEE. <https://doi.org/10.1109/ICInfA.2013.6720443>.
  9. Gieras, J. F. (2008). *Advancements in electric machines*. Springer Science & Business Media.
  10. Ma, L., Wang, D., Zhang, Y., Wang, L., Lv, P., & Sun, Y. (2014). 3D path planning of a laser manipulation robotic system for tooth preparing. In *2014 IEEE international conference on robotics and automation (ICRA)* (pp. 1922–1928). IEEE. <https://doi.org/10.1109/ICRA.2014.6907113>.
  11. Vollborn, T., Habor, D., Junk, S., Radermacher, K., & Heger, S. (2012). A voice-coil actuated ultrasound micro-scanner for intraoral high resolution impression taking. In *2012 IEEE/RSJ international conference on intelligent robots and systems* (pp. 3571–3576). IEEE. <https://doi.org/10.1109/IROS.2012.6385973>.
  12. Schlamminger, S. (2012). Design of the permanent-magnet system for NIST-4. *IEEE Transactions on Instrumentation and Measurement*, 62(6), 1524–1530. <https://doi.org/10.1109/TIM.2012.2230771>
  13. Sutton, C. M., & Clarkson, M. T. (2014). A magnet system for the MSL watt balance. *Metrologia*, 51(2), S101. <https://doi.org/10.1088/0026-1394/51/2/S101>
  14. Okyay, A., Khamesee, M. B., & Erkorkmaz, K. (2015). Design and optimization of a voice coil actuator for precision motion applications. *IEEE Transactions on Magnetism*, 51(6), 1–10. <https://doi.org/10.1109/TMAG.2014.2381160>
  15. Dong, L., Chen, J., Zhang, C., Wu, D., & Yu, G. (2015). A novel voice coil motor used in nano-positioning device. In *2015 18th international conference on electrical machines and systems (ICEMS)* (pp. 1997–2002). IEEE. <https://doi.org/10.1109/ICEMS.2015.7385368>.
  16. Luo, C., Sun, J., Liao, Y., & Xu, S. (2019). Analysis and design of ironless toroidal winding of tubular linear voice coil motor for minimum copper loss. *IEEE Transactions on Plasma Science*, 47(5), 2369–2375. <https://doi.org/10.1109/TPS.2018.2890690>
  17. Roters, H. C. (1941). *Electromagnetic devices*. J. Wiley & sons, Incorporated.
  18. <https://www.sensata.com/sites/default/files/a/sensata-linear-actuator-LA-10-12-drawing.pdf>.
  19. Luo, C., Sun, J., Wang, X., & Shen, Q. (2017). Design of voice coil motor with the forward winding for linear vibro-impact systems. *IEEE Transactions on Magnetism*, 53(8), 1–9. <https://doi.org/10.1109/TMAG.2017.2694395>
  20. Luo, C., Li, X., Liao, Y., & Long, X. (2020). Design of end-iron-free voice coil motor with appropriate PM length ratio. *IEEE Transactions on Energy Conversion*, 35(2), 1139–1146. <https://doi.org/10.1109/TEC.2020.2973308>

**Publisher's Note** Springer Nature remains neutral with regard to jurisdictional claims in published maps and institutional affiliations.

Springer Nature or its licensor (e.g. a society or other partner) holds exclusive rights to this article under a publishing agreement with the

author(s) or other rightsholder(s); author self-archiving of the accepted manuscript version of this article is solely governed by the terms of such publishing agreement and applicable law.



**Sunghoon Kang** received his B.S., M.S., and Ph.D. degrees from the Department of Mechanical Engineering of the Korea Advanced Institute of Science and Technology (KAIST), Republic of Korea, in 2002, 2004, and 2011, respectively. He was a Senior Researcher at Samsung Electronics, Suwon, Republic of Korea, where he worked on multi-energy X-ray imaging for mammography. He was an Associate Research Engineer at the Department of Mechanical Engineering of the Ajou University,

Suwon, Republic of Korea, where he worked on high-precision positioning stages. He is currently an Assistant Professor at the Department of Mechanical and Control Engineering of the Seoul Cyber University, Seoul, Republic of Korea. His research interests include the design of high-precision positioning systems and medical imaging systems.



**Yong-Gon Jeong** received his B.S. and M.S. degrees from the Department of Mechanical Engineering of the Ajou University, Suwon, Republic of Korea, in 2018 and 2020, respectively. He is currently working on the mechanical design of surgical robot at Kohyoung Technology, Yongin, Republic of Korea. His research interests include the design and control of miniaturized actuators for multi-purpose robots.



**Young-Man Choi** received his B.S., M.S., and Ph.D. degrees from the Department of Mechanical Engineering of the Korea Advanced Institute of Science and Technology (KAIST), Republic of Korea, in 2002, 2004, and 2008, respectively. He is an Associate Professor at the Department of Mechanical Engineering of the Ajou University, Suwon, Republic of Korea. From 2008 to 2011, he worked at the National Institute of Standards and Technology (NIST), United States, where he worked on a

project on MEMS nano-positioning and metrology systems for NEMS/MEMS. From 2012 to 2016, he was a Senior Researcher at the Korea Institute of Machinery and Materials (KIMM), Daejeon, Republic of Korea, where he worked on precision machines and processes for printed flexible electronics. His research interests include high-precision machines and biomechanical devices.